

Cite this: *J. Mater. Chem. A*, 2023, **11**, 4272

First-principles study on ultrafast Li-ion diffusion in halospinel $\text{Li}_2\text{Sc}_{2/3}\text{Cl}_4$ through multichannels designed by aliovalent doping[†]

Suseong Hyun,^a Hoje Chun,^{‡a} Minjoon Hong,^a Joonhee Kang^b and Byungchan Han^{*,a}

Solid electrolytes have attracted considerable interest as next-generation materials for lithium-ion batteries because their chemical stability is incomparably higher than that of conventional liquid-phase electrolytes. However, the issue of slow Li^+ diffusion, even in advanced halide-type electrolytes, still needs to be resolved. Here, we report the design of ultrafast diffusion channels for Li ions through optimal aliovalent doping (Fe^{2+}) of the halide electrolyte with a chloride framework. Both first-principles density functional theory calculations and *ab initio* molecular dynamics simulations consistently demonstrate that the proposed material has high chemical stability and high Li-ion conductivity. We noted that the Fe dopant creates multichannels for Li ion diffusion, which is ascribed to the favorable regulation of electrostatic interaction with the concertedly moving Li ions. Our calculations indicate that the ionic conductivity of the proposed material is up to 2.72 mS cm^{-1} , which is a very competitive value considering that conventional organic ionic conductors show values around 1.0 mS cm^{-1} . We clearly unveil the underlying mechanism of outstanding performance, which is cost-effective and may be used for fabricating even better solid electrolytes.

Received 9th December 2022
Accepted 20th January 2023

DOI: 10.1039/d2ta09592k

rsc.li/materials-a

Introduction

Lithium-ion batteries (LIBs) are widely used as electrochemical energy storage and power systems in appliances ranging from portable electronic devices to large electric vehicles.^{1,2} Despite their high energy and power densities, LIBs have relatively low chemical stability, occasionally leading to fires and even human casualties.³ The accidents have strongly driven the replacement of conventional liquid-phase organic electrolytes with solid electrolytes (SEs).^{4–8} SEs allow more flexibility in the use of high-energy materials such as Li metal for anodes and high-Ni cathodes, resulting in improved energy density and chemical stability.

The key issue with SEs is their much lower Li-ion conductivity than liquid organic electrolytes ($\geq 10 \text{ mS cm}^{-1}$).^{9,10} Over the last several decades, extensive research and design of SEs with anion frameworks, including oxides ($\text{Li}_7\text{La}_3\text{Zr}_2\text{O}_{12}$ ¹¹ and $\text{Li}_{1.3}\text{Al}_{0.3}\text{Ti}_{1.7}(\text{PO}_4)_3$ (ref. 12)) and sulfides ($\text{Li}_{10}\text{GeP}_2\text{S}_{12}$ ¹³ and $\text{Li}_7\text{P}_3\text{S}_{11}$ (ref. 14)), have been attempted using costly and time-

consuming experimental and theoretical approaches. As oxide SEs rarely met the desired levels of mechanical performance and ionic conductivity,¹⁵ sulfide SEs have attracted considerable attention¹⁶ because of their excellent mechanical deformability even by cold pressing and desirable interface formation with the electrodes in LIBs. However, sulfide SEs were found¹⁷ to be seriously problematic because of the generation of toxic H_2S gas under humid conditions.

Halide SEs with a chlorine framework have attracted considerable attention owing to several excellent properties: a wide electrochemical operation window, good stability in air and under humid conditions, and few side reactions. Notably, these materials have been significantly developed: their ionic conductivity ($\sim 10^{-2} \text{ mS cm}^{-1}$)¹⁸ has been increased to the commercial level ($> 1 \text{ mS cm}^{-1}$),^{19–25} particularly in Li_3ErCl_6 , Li_3YCl_6 , Li_3InCl_6 , and Li_3ZrCl_6 crystals. Trigonal, orthorhombic, monoclinic, and cubic spinel-type halide SEs, so-called halospinel (*e.g.*, $\text{Li}_2\text{Sc}_{2/3}\text{Cl}_4$), may be prepared *via* a relatively simple process and exhibit high ionic conductivity and outstanding oxidation stability.

Even though they have high ionic conductivities, most halide SEs utilize costly rare-earth metals. Various strategies have been proposed for the development of cost-effective methods for increasing ionic conductivity.^{21,26,27} In particular, cation or anion doping was attempted. For instance, Kwak²³ pursued mechanism studies on the aliovalent substitution of Fe^{3+} for Zr^{4+} in Li_3ZrCl_6 and reported substantial improvements in ionic

^aDepartment of Chemical and Biomolecular Engineering, Yonsei University, Seoul 03722, Republic of Korea. E-mail: bchan@yonsei.ac.kr^bDepartment of Nanoenergy Engineering, Pusan National University, Busan, 46241, Republic of Korea[†] Electronic supplementary information (ESI) available. See DOI: <https://doi.org/10.1039/d2ta09592k>[‡] Equal contribution.

conductivity due to the lower oxidation state of Fe^{3+} and enhanced covalency because of the doping. As an extension of the approach, multiple-elemental doping has been attempted for a more substantial improvement in Li-ion conductivity through crystal structural distortion to aid Li^+ diffusion. For example, Nazar²⁸ demonstrated that aliovalent substitution of Sc^{3+} in $\text{Li}_2\text{Sc}_{2/3}\text{Cl}_4$ for In^{3+} should improve the Li^+ conductivity up to 2.0 mS cm^{-1} . At high In^{3+} dopant concentrations, the crystal structure is severely distorted to form a monoclinic phase because In^{3+} has a larger ionic radius than Li^+ . Notably, promising cationic dopants have already been identified through high-throughput computational screening,^{29,30} but the effect of each dopant on Li^+ diffusion and the mechanism of this effect have not yet been elucidated.

In this study, we applied first-principles density functional theory (DFT) calculations and *ab initio* molecular dynamics (AIMD) simulations to unveil the mechanism of the modification of the thermodynamic and kinetic properties of halospinel $\text{Li}_2\text{Sc}_{2/3}\text{Cl}_4$ (LSC) SEs through Fe^{2+} doping. Iron is one of the most abundant elements in the Earth, and it is more than three orders of magnitude more abundant than Sc.³¹ Based on experimentally reported halospinel SE (LSC) we set up three different models: LSC, $\text{Li}_{18}\text{Sc}_4\text{FeCl}_{32}$, and $\text{Li}_{19}\text{Sc}_3\text{Fe}_2\text{Cl}_{32}$ (denoted by LSC- $x\text{Fe}$, where $x = 0.2$ or 0.4 is a molar ratio) with different stoichiometries and configurations. LSC-0.2Fe (2.72 mS cm^{-1}) showed considerably higher Li-ion conductivity than LSC (2.07 mS cm^{-1}) at room temperature (300 K). Using ion correlation analysis, we confirmed that this outstanding behavior originates from the collective concerted motion of Li ions in multi-diffusional channels. The bonding nature in the anion framework revealed that Fe^{2+} -doping provided higher degrees of freedom for the motion of Li ions and shielded them from electrostatic attraction toward anions.

Methods

First-principles DFT calculations were performed using the Vienna *ab initio* simulation package³² with the implemented projector augmented wave pseudo-potential.³³ The Perdew–Burke–Ernzerhof functional was adopted by the generalized-gradient approximation method to describe the exchange–correlation energy of the electrons.³⁴ The cutoff energy for expanding plane-wave basis functions was 520 eV, and the Brillouin zone in the reciprocal space with the Monkhorst–Pack scheme was sampled using $4 \times 4 \times 4$ k -points. All structures were optimized until the spin-polarized total energy and force converged within 10^{-5} eV and 0.02 eV \AA^{-1} , respectively. The GGA + U method was applied to Fe with an effective parameter of 3.29 eV.³⁵ The formation energy (ΔG_f) was calculated to obtain the thermodynamically most stable structure for the selected configurations, as expressed in eqn (1):

$$\Delta G_f = E_{\text{LSC-0.2xFe}} + xE_{\text{Sc}} - E_{\text{LSC}} - x(E_{\text{Li}} + E_{\text{Fe}}) \quad (1)$$

where $x = 1$ or 2 and E_z stands for the average DFT energy for structure Z .

AIMD simulations were conducted under the computational conditions of the Nosé–Hoover thermostat with fixed volume, temperature, and number of particles. The time step of the AIMD simulations was 2 fs and overall 50 000 steps were run at different temperatures, ranging from 600 to 1200 K with 100 K intervals at a Γ -point.³⁶ Atomic trajectories were analyzed using Pymatgen,³⁷ and the activation energy along the Li^+ diffusion path was evaluated *via* the climbing-image nudged elastic band method.³⁸ The diffusion coefficient for Li ions was calculated through the linear fitting of mean square displacement (Fig. S6†) as a function of time for each considered temperature. The ionic conductivity using the Nernst–Einstein relation was determined as expressed in eqn (2):

$$\sigma = \frac{\rho z^2 F^2}{RT} D \quad (2)$$

where ρ and z represent the molar density and the charge of Li^+ in a unit cell, respectively; F and R are the Faraday constant and gas constant, respectively. The overall activation energy of Li ion diffusion was evaluated using the Arrhenius relationship, assuming that no phase transitions occurred and plentiful defect carriers were present at all studied temperatures.³⁶ The equation is given by eqn (3):

$$D = D_0 \exp\left(-\frac{E_a}{kT}\right) \quad (3)$$

where D_0 is the diffusivity at $T \rightarrow \infty$ and k is the Boltzmann constant.

The ratio of correlated jump analysis for the AIMD simulation data was conducted as illustrated by Klerk *et al.*³⁹ Concerted motions can be obtained when two hopping events occurred simultaneously in the one atomic vibration period, defined as the reciprocal value of the attempt vibration.⁴⁰ The 8a, 16c, and 16d sites were treated as available for Li to occupy the positions, and the temporal criterion was set to 0.12 ps and the spatial criterion was set to 5 \AA for covering all available concerted Li hoppings.

Results and discussion

Construction of model systems

We set up computational models by adapting experimentally synthesized spinel structure, LSC.²⁴ Its structure consists of corner-sharing crystal frameworks with minimal electrostatic repulsion among the cations to foster fast Li^+ transport.⁴¹ There are four Wyckoff sites for Li^+ to occupy: 8a, 16c, 16d, and 48f, and each of the sites is corner-sharing, edge-sharing, and face-sharing (Fig. 1a and Table S1†). The dopant Fe^{2+} was allocated to a Sc^{3+} site.

One of the atomic sites available for excess Li, the 16c, shares faces with 8a (tetrahedral) and 48f (tetrahedral), whereas the 48f site shares faces with the octahedral ones, 16c and 16d. The 16c and 48f sites are thermodynamically infeasible for deploying excess Li^+ atoms because of the shorter central ionic distances and increased electrostatic repulsion.⁴² Based on this, we selected 8a and 16d to form Li-polyhedra with corner- or edge-sharing structures. This consideration is consistent with

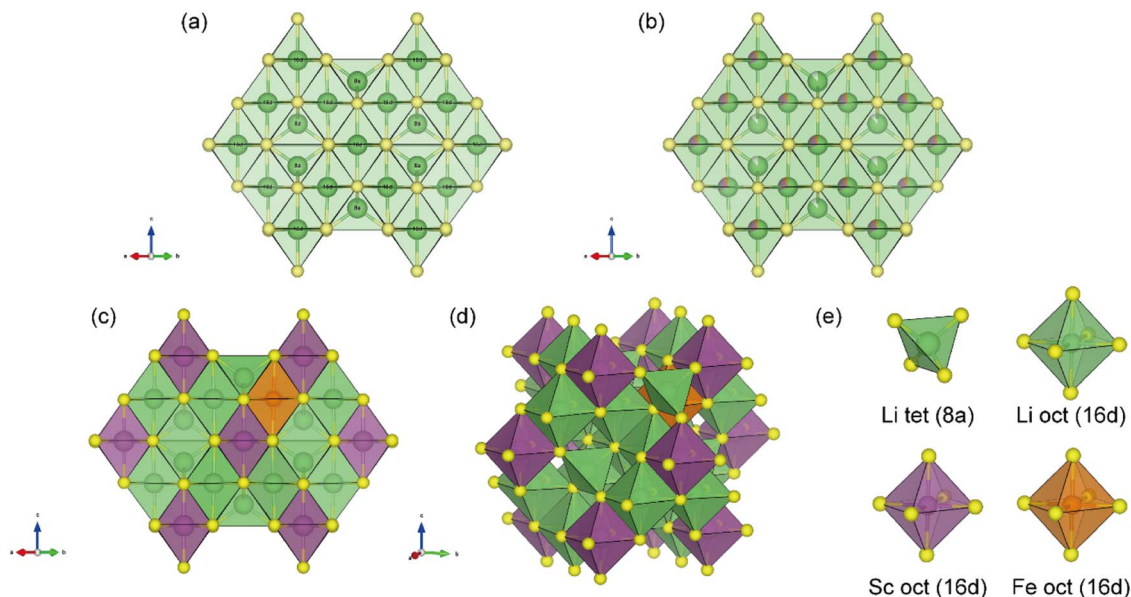


Fig. 1 Model systems of Fe-doped $\text{Li}_2\text{Sc}_{2/3}\text{Cl}_4$, (a) 8a and 16d sites for Li occupation in the spinel structure. (b) The accommodation of Li and Sc in the structure. Both Li and Sc sharing the 16d site. (c) and (d) The most thermodynamically stable structure for LSC-0.2Fe and (e) its components.

a previous report by Zhou,²⁴ in which the measured isotropic displacement parameters (8a for Li^+ and 16d for Li^+ and Sc^{3+} with no face sharing connectivity) confirmed that the 16d site forms a stable rigid framework.

Fe can also occupy all Wyckoff sites of spinel, so we evaluated the most preferable site of Fe^{2+} doping as shown in Fig. S1 and Table S2.†

The doping energy revealed that the 16d site is the most stable site of Fe^{2+} doping. Fe^{2+} is a d^6 metal, so it has a negative octahedral site preference energy (OPSE), which means that Fe^{2+} tends to form an octahedral framework. Additionally, the ionic radius of Fe^{2+} is slightly larger than that of Sc^{3+} and thus it is more likely for Fe^{2+} to occupy an octahedral site than a tetrahedral site. Both 16c and 48f sites were formed to share the Li 16d or 8a site, resulting in high doping energy. Therefore, we constructed model systems of LSC-0.2Fe and LSC-0.4Fe from LSC by chemical doping with Fe^{2+} at 16d (replacing Sc^{3+}) and additional Li^+ at the 8a vacant site to maintain charge balance. Therefore, the occupancies at the 8a and 16d sites in LSC-0.2xFe ($x = 1, 2$) are as follows: the 8a site has an occupancy of $(0.75 + 0.125x) \text{Li}^+$, whereas the 16d site has an occupancy of 0.6875Li^+ , $(0.3125 - 0.0625x) \text{Sc}^{3+}$, and $0.0625x \text{Fe}^{2+}$, respectively.

Meanwhile, doping transition metal Fe with varying oxidation states may induce another scenario, doping trivalent Fe. We calculated the doping energy of LSC-0.2Fe by considering both Fe^{3+} and Fe^{2+} doping and showed that the doping energy of Fe^{3+} was twice as much as that of Fe^{2+} (Table S3†). Unlike Fe^{2+} , the ionic radius of Fe^{3+} (0.645 \AA) is smaller than that of Sc^{3+} (0.78 \AA). This can induce structural distortion, leading to thermodynamic instability. The average cation distortion index also reveals the instability of Fe^{3+} doping (0.025 for Fe^{2+} doping and 0.030 for Fe^{3+} doping, respectively). Thus, we only considered divalent Fe to construct LSC-0.2Fe and LSC-0.4Fe.

Using the Supercell⁴³ program, we generated a total of 100 000 structures with different contents of Fe and Li atoms, as shown in Fig. 1b. Instead of performing DFT calculations for all structures, we focused on specific configurations that have Fe at only 16d sites with sparse cation distributions and thereby may exhibit fast Li-ion diffusion.⁴⁴

We selected 39 structures for LSC-0.2Fe and 33 for LSC-0.4Fe. Fig. S2† illustrates the energy differences between the chosen 39 and 33 structures and the most stable structures (Fig. S2a and b†), which are the 25th structure (Fig. S2c†) for LSC-0.2Fe of the Fe–Sc polyhedron adjoined by edge-sharing and the 22nd structure (Fig. S2e†) for LSC-0.2Fe of the Fe polyhedron, which is far from another cation polyhedron. Notably, both have similar cation distributions, but the formation energy differs by as much as 0.72 eV. Such a difference was attributed to Fe^{2+} , which has a lower oxidation number than Sc^{3+} and thus effectively decreases the electrostatic repulsion between edge-sharing cations. The same is observed for the 26th and 31st structures in LSC-0.4Fe (Fig. S2d and f†). Furthermore, thermodynamic stability can be affected by the configuration of the vacant 8a site. Among the 19th, 25th, 27th, and 30th structures, which have similar thermodynamic stabilities and the same cation distribution, only the 25th structure has a vacant 8a site around the Fe octahedron. Fe^{2+} (0.78 \AA) is larger than Sc^{3+} (0.745 \AA) and thus induces a severer structural distortion as additional Li octahedra form asymmetrical bonds. Similarly, LSC-0.2Fe shows that the Fe–Sc polyhedron with edge-sharing neighbors is the most thermodynamically stable, whereas an isolated Fe polyhedron that does not share any cation polyhedron is the most unstable. As the excess Li ions occupy all vacant 8a sites and also induce structural distortion, the thermodynamic structural stability difference between the most stable and the most unstable structures in LSC-0.4Fe is up to 0.87 eV, which is

significantly higher than that in the LSC-0.2Fe structure (0.72 eV).

Li⁺ passing through the gate

As shown in Fig. 1a, Li⁺ diffuses through only 16d (octahedral) sites. This means that the fully connected 3-dimensional diffusion network may be eventually blocked by the cations (*e.g.*, Sc³⁺ and Fe²⁺) located at the same Wyckoff sites. The short atomic displacement, 0.0029 Å² for 16d and 0.025 Å² for 8a sites, supports the argument.²⁴ Therefore, additional diffusion channels through other Wyckoff sites are necessary to ensure high Li⁺-conductivity, for example, through Li⁺ hopping from 16d to 8a or 48f in nearby tetrahedra.

To evaluate whether the dopant Fe²⁺ creates transport channels favorable for Li⁺ diffusion, we calculated probability density distributions of Li⁺ at 800 K in LSC and LSC-0.2Fe. As shown in Fig. 2a (LSC) and 2b (LSC-0.2Fe), both diffusion channels are three-dimensional. However, the region around the Fe octahedra (marked with a black box in Fig. 2b) shows a significantly higher probability density. This implies much tighter connectivity between spaces, leading to faster Li ion diffusion. We calculated the migration barrier for Li ions along the diffusion paths, wherein the channels have a void centered by six surrounding octahedra. For convenience, we called the diffusion path a 'gate' and the center a 'gate site'. Among the various types of gates and gate sites, we selected a specific gate containing Fe²⁺ (Fig. S3†) and set two 8a sites instead of one as a starting position of the migrating Li⁺ to characterize the concerted motion of Li ions during diffusion.

The energy profile through the gate site is illustrated in Fig. 3a with a corresponding migration pathway shown in Fig. 3b. The energy profile appears symmetrically in both LSC and LSC-0.2Fe structures. However, the detailed mechanisms of Li⁺ diffusion along the pathway are significantly dissimilar. The intermediate state, where Li⁺ occupies the gate site (5th image),

in LSC-0.2Fe is significantly more stable than that in LSC. As Li⁺ migrates into the gate (from the 3rd to the 5th images), LSC-0.2Fe shows a much lower activation energy (0.206 eV) than the LSC structure (0.288 eV). It was ascribed to a larger ionic radius and a lower oxidation number of Fe²⁺ compared to Sc³⁺. This considerably promoted Li⁺ hopping to the gate site. As Li⁺ moves out of the gate site (from the 7th to the 9th images), LSC-0.2Fe shows an activation energy of 0.303 eV, which is slightly higher than that for LSC (0.292 eV). Fig. S4† also confirms that there is a low energy barrier for entering and high energy barrier for escaping the gate. That is, the dopant Fe²⁺ provides pathways with low activation energy for Li⁺ to diffuse into the gate site but also a high energy barrier to escape the site.

Notably, the 5th image of the LSC-0.2Fe exhibits the same energy as the initial site (1st image), implying that the gate site can work for a new Li⁺ hop. Otherwise, the cation blocks the Li octahedron linking the new channel, and the octahedra are actively linked promoting fast Li⁺ diffusion (Fig. S5†).

Effects of aliovalent doping

We evaluated the role of dopant Fe²⁺ on Li⁺ migration using Bader charge analysis and the electron localized function (ELF), which allows acquiring the probability that an electron pair is localized in the specific chemical bonding region (Fig. 4a–c). For Li⁺, the charge distribution seems upshifted, meaning that more electrons are located near the moving Li⁺. Similarly, Cl ions also decrease the charge. We estimated the electrostatic interaction between the migrating Li⁺ and nearby Cl⁻ based on ionic charges (Q_{Li^+} , Q_{Cl^-}) and interatomic distance ($d_{\text{Li}^+-\text{Cl}^-}$), as shown in Table S4.† The results indicate that Li⁺ migrates into the gate under strong electrostatic attraction from Cl⁻ in the Fe²⁺-doped structure. The ELF indicates that the chemical bond between Li⁺ and Cl⁻ (the 4th image in Fig. S4†) is largely ionic⁴⁵ (note that the probability is lower in the interatomic region).

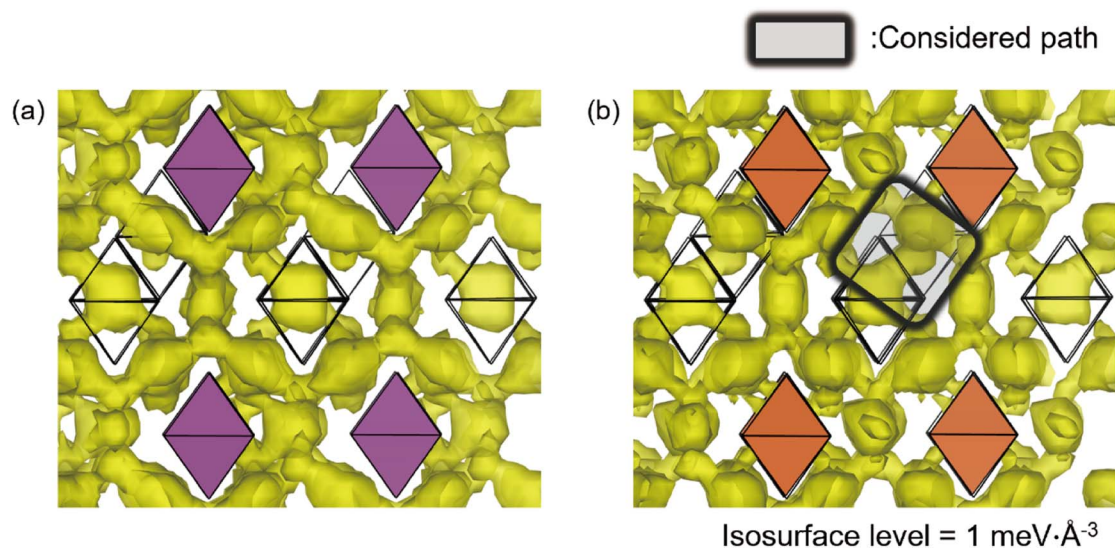


Fig. 2 Probability density distribution of Li ions obtained using AIMD simulations at 800 K. The yellow regions represent the regions where Li ions may reside for (a) LSC and (b) LSC-0.2Fe, respectively.

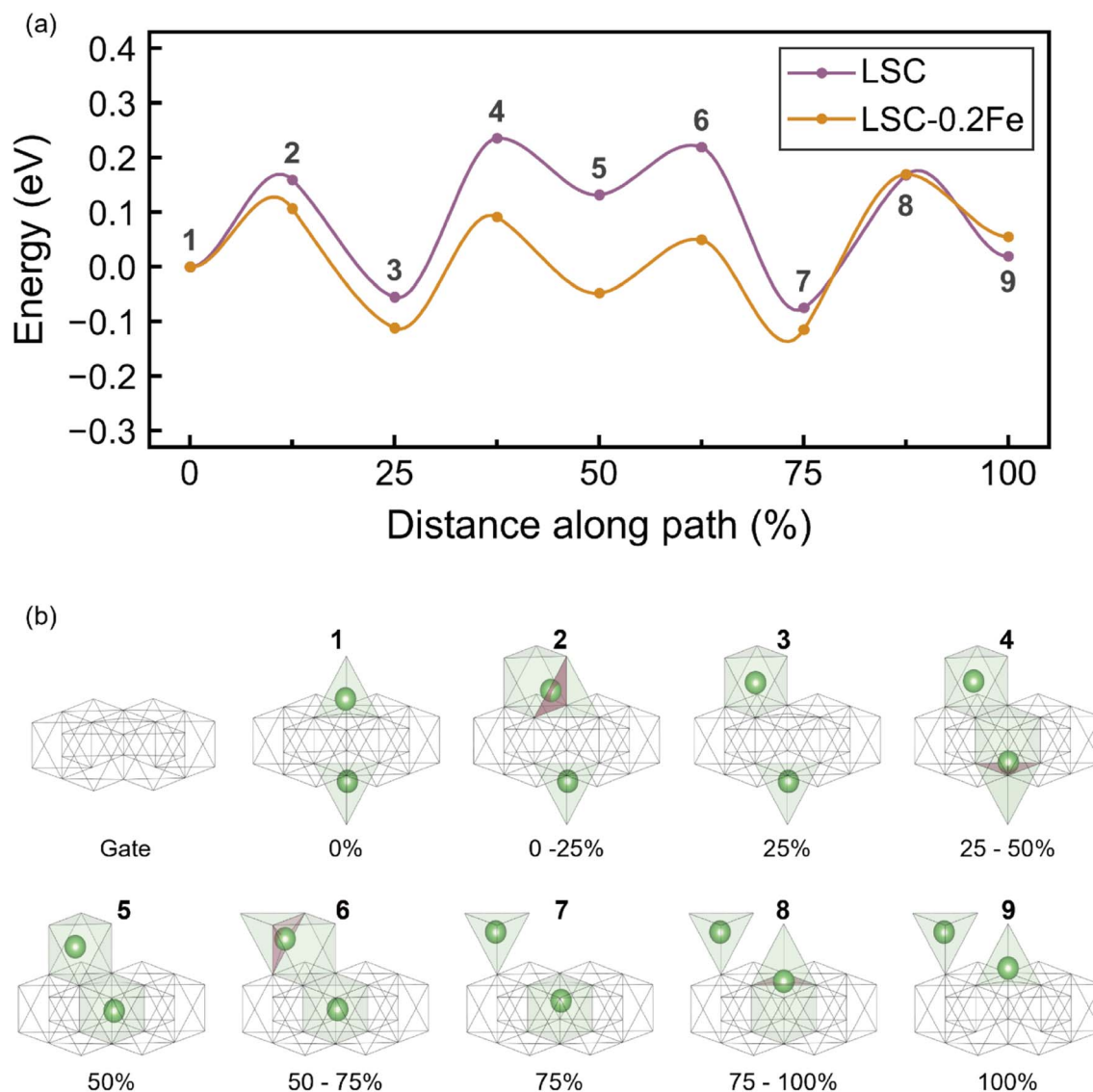


Fig. 3 Li ion migration pathways from nudge elastic band (NEB) calculations. (a) Energy profile of the pathways in LSC (purple) and LSC-0.2Fe (orange) corresponding to the migration distance along the paths. (b) The image of the intermediate step during migration. The triangular faces are colored pink if Li^+ migrated through the tetrahedron site to the octahedron site and *vice versa*. The other pathway (more unfavorable) is illustrated in Fig. S4.†

Fig. 4c reveals that the ionicity is higher in LSC-0.2Fe, leading to stronger attraction of diffusing Li^+ .

While the charge variation for Li^+ is negligible, Cl^- is considerably polarized up to almost -1.0 . Additionally, the electron probability in the ELF is shifted toward Cl^- because Cl^- is free from interaction with cations because of its lower oxidation number compared to Fe^{2+} . Furthermore, the distortion index⁴⁶ at $[\text{ScCl}_6]^{3-}$ and $[\text{FeCl}_6]^{4-}$ (0.036 *versus* 0.049, respectively) shows the enhancement in Li^+ diffusion with the Fe-doping.

Li-ion conductivity in the Fe-doped halospinel

Although 8a-to-8a site migration of Li^+ is thermodynamically implausible in LSC-Fe, overall diffusion may increase owing to the thermodynamic stabilization of the gate site and the

formation of new structural connectivity along the diffusion planes in LSC-0.2Fe. Using AIMD simulations for LSC, LSC-0.2Fe, and LSC-0.4Fe, we determined the effect of the dopant Fe^{2+} on Li^+ diffusion. Specifically, we calculated dynamical data and ionic conductivity over Li^+ diffusion (Fig. 5). Calculated Li-ion conductivities in LSC, LSC-0.2Fe, and LSC-0.4Fe are 2.07, 2.72, and 0.34 mS cm^{-1} and the activation energies are 0.277, 0.266, and 0.342 eV, respectively.

Notably, Li-ion conductivity is the highest in LSC-0.2Fe. LSC-0.4Fe shows lower ionic conductivity, even though it has a higher Fe^{2+} content. This is surprising because LSC-0.4Fe should have more Li^+ diffusion channels and more effective charge carriers than LSC-0.2Fe according to the above speculations. Furthermore, such results are consistent with those of an experimental report²³ on a similar anion framework. To

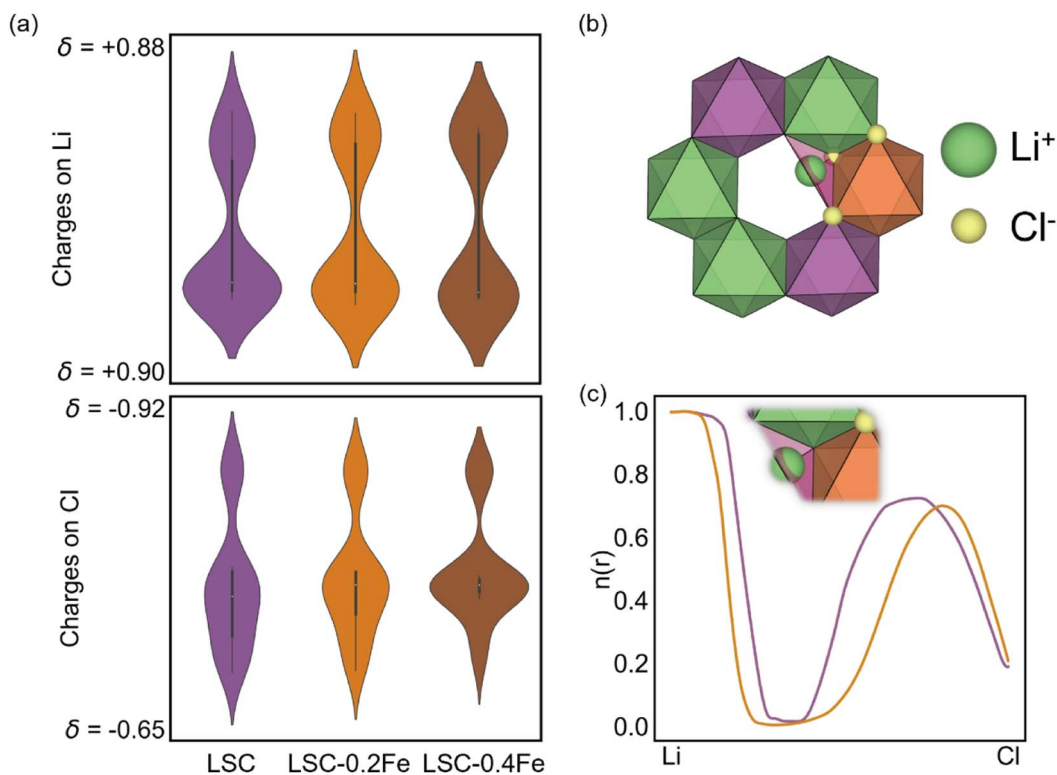


Fig. 4 Bader charge and ELF results. (a) Charge distributions of Li⁺ (upper) and Cl⁻ (below) obtained from the Bader charge analysis of the most thermodynamically stable structure of LSC-0.2Fe. (b) Schematic of the location of Cl⁻ in [FeCl₆]⁴⁻ and migrating Li⁺, obtained from the 4th image of the migration path shown in Fig. S4.† (c) ELF analysis for Cl⁻ and Li⁺.

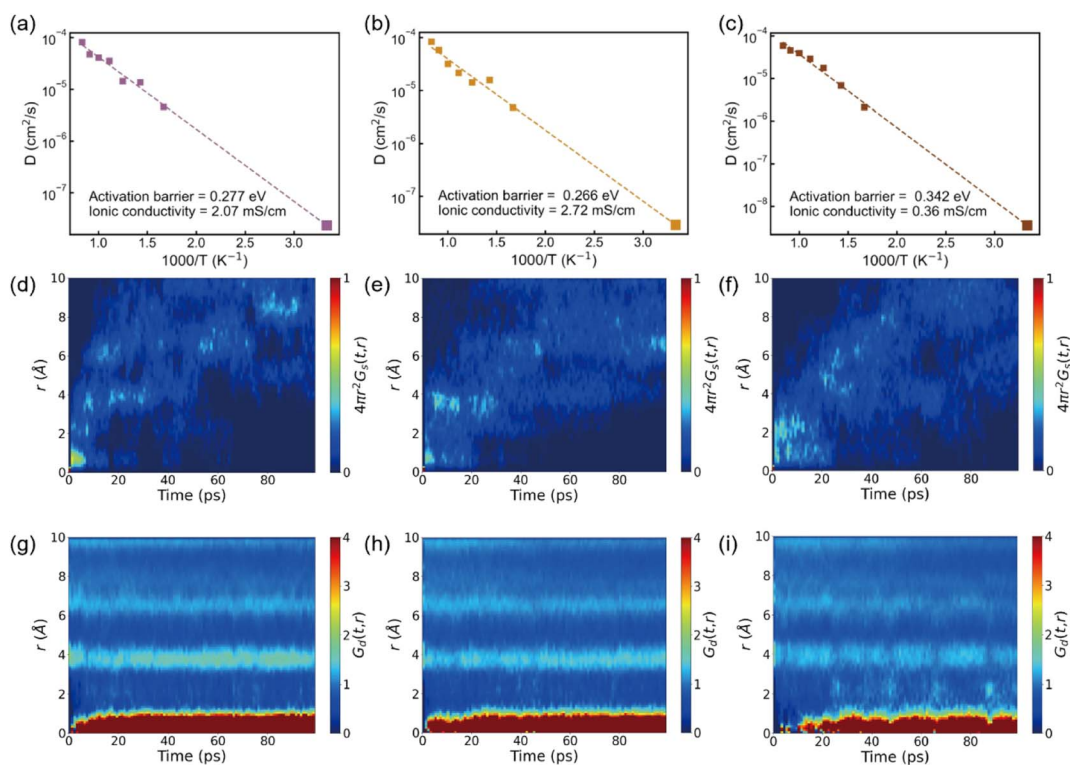


Fig. 5 AIMD analysis. (a)–(c) Arrhenius plots for LSC, LSC-0.2Fe, and LSC-0.4Fe, respectively. 2D heatmaps for (d)–(f) the self-part (G_s) and (g)–(i) the distinct part (G_d) of the van Hove correlation functions of Li⁺ at 800 K for 100 ps of AIMD simulation.

explain this tendency, we analyzed the motion of Li^+ using the van Hove correlation function.³⁶ The self-part (G_s) and distinct-part (G_d) of the van Hove function were calculated using eqn (4) and (5), respectively, using the trajectories of diffusing Li^+ obtained by AIMD simulations at 800 K.

$$G_s(r, t) = \frac{1}{4\pi r^2 N_d} \left\langle \sum_{i=1}^{N_d} \delta(r - |r_i(t_0) - r_i(t + t_0)|) \right\rangle_{t_0} \quad (4)$$

$$G_d(r, t) = \frac{1}{4\pi r^2 \rho N_d} \left\langle \sum_{i \neq j}^{N_d} \delta(r - |r_i(t_0) - r_j(t + t_0)|) \right\rangle_{t_0} \quad (5)$$

The self-part is the probability density of an ion diffusing within time t from its initial site to another site at a distance r . So, if the red peak fades away as quickly as possible, the material is a fast ionic conductor. The distinct-part indicates the radial distribution of the transporting ions with respect to the initial ion. That is, if the peak appears as early as possible, the collective Li^+ motion is more likely to occur. Among the three halospinel models, LSC-0.2Fe shows the fastest Li-ion hopping to the next sites. The considered Li hopping site in this work and each distance in the halospinel are listed in Table S5.† Furthermore, it is noteworthy that there is a peak at around 4 Å in the self-part (Fig. 5e), meaning that the octahedron-to-octahedron diffusion occurs more frequently because new links were formed by the dopant Fe^{2+} and the extra Li^+ (Fig. S5†). However, in LSC-0.4Fe, there is a wide peak distributed across 0–4 Å (Fig. 5f), which can be interpreted as Li^+ residing at the gate site without escaping. The more Fe^{2+} is doped, the more it attracts Li^+ . In the distinct part, LSC-0.2Fe (Fig. 5h) demonstrates good collective motion similar to LSC (Fig. 5g) because the peak at around $r = 0$ Å appears almost the same. The red peak emerges almost immediately for both LSC and LSC-0.2Fe and only after 20 ps for LSC-0.4Fe (Fig. 5i). To quantitatively unveil the concerted motion of Li^+ , the total number of total concerted hoppings of Li^+ was investigated (Fig. S7†). The overall concerted motion showed a similar tendency to the outcome of AIMD, with the highest ionic conductivity at LSC-0.2Fe and the lowest at LSC-0.4Fe. This can be explained by the number of collective hoppings that are only octahedron to octahedron hoppings. In LSC-0.2Fe, the concerted motion with octahedron-to-octahedron diffusion was quite increased, because the gate site was transformed into the preferred site notwithstanding the formation of face sharing. For LSC-0.4Fe, however, the gate site rather entrapped the migrating Li^+ , resulting in reduced octahedron diffusion.

Furthermore, we analyzed the percentage of single Li^+ jump events from the octahedron to the octahedron and the results are displayed in Fig. S8.† As it becomes facile for migrating Li^+ to occupy the gate site by Fe ions, the Li^+ hopping from octahedron to octahedron may occur more frequently, resulting in high ionic conductivity. Fig. S8† also shows a similar tendency for the ionic conductivity of each structure. Our results show similar trends to the previous study by Yoon and co-workers²³ that the optimal content of doping Fe in similar halide SSE was found to be around 0.2. In summary, Fe^{2+} -doping facilitates Li^+

migration and significantly improves the ionic conductivity; at the same time, excessive Fe^{2+} can strongly trap Li^+ , thereby reducing ionic conductivity. Thus, the rational design of highly ion conductive halospinel electrolytes requires careful selection of the types and concentrations of cations.

Conclusions

We designed a superionic solid electrolyte for Li diffusion *via* Fe-doping of $\text{Li}_2\text{Sc}_{2/3}\text{Cl}_4$. DFT calculations yielded an ionic conductivity of up to 2.72 mS cm^{-1} for LSC-0.2Fe. The underlying mechanism is the formation of multi-diffusion channels with tight topological connectivities between octahedra along the Li migration paths, which are absent in undoped LSC electrolyte. DFT calculations indicate that the dopant Fe^{2+} played a crucial role in promoting Li^+ to occupy the gate site and thus aided the formation of bonding networks between Li octahedra, leading to the generation of multi-diffusion channels. Furthermore, because the dopant Fe^{2+} has a lower oxidation state than Sc^{3+} , its mutual electrostatic attraction with Cl^- and Li^+ should be much stronger.

However, as the doping concentration was increased further (LSC-0.4Fe), Li^+ was trapped in the gate site because of the strong bonding with Cl^- , which reduced Li ionic conductivity. This study provides design principles for exploring promising candidates and fabricating highly active solid electrolytes towards Li ion diffusion, which has been a long-standing issue for next-generation LIBs.

Conflicts of interest

There are no conflicts to declare.

Acknowledgements

This research was mainly supported by the National Research Foundation of Korea (2022M3H4A1A04096482) funded by the Ministry of Science and ICT.

References

- 1 J.-M. Tarascon and M. Armand, in *Materials for sustainable energy: a collection of peer reviewed research and review articles from Nature Publishing Group*, World Scientific, 2011, pp. 171–179.
- 2 M. Armand and J.-M. Tarascon, *Nature*, 2008, **451**, 652–657.
- 3 Q. Wang, P. Ping, X. Zhao, G. Chu, J. Sun and C. Chen, *J. Power Sources*, 2012, **208**, 210–224.
- 4 R. Chen, Q. Li, X. Yu, L. Chen and H. Li, *Chem. Rev.*, 2019, **120**, 6820–6877.
- 5 S. Randau, D. A. Weber, O. Kötz, R. Koerver, P. Braun, A. Weber, E. Ivers-Tiffée, T. Adermann, J. Kulisch and W. G. Zeier, *Nat. Energy*, 2020, **5**, 259–270.
- 6 J. Janek and W. G. Zeier, *Nat. Energy*, 2016, **1**, 1–4.
- 7 Y.-S. Hu, *Nat. Energy*, 2016, **1**, 1–2.

- 8 Z. Zhang, Y. Shao, B. Lotsch, Y.-S. Hu, H. Li, J. Janek, L. F. Nazar, C.-W. Nan, J. Maier and M. Armand, *Energy Environ. Sci.*, 2018, **11**, 1945–1976.
- 9 A. Manthiram, X. Yu and S. Wang, *Nat. Rev. Mater.*, 2017, **2**, 1–16.
- 10 T. Zhang, W. He, W. Zhang, T. Wang, P. Li, Z. Sun and X. Yu, *Chem. Sci.*, 2020, **11**, 8686–8707.
- 11 R. Murugan, V. Thangadurai and W. Weppner, *Angew. Chem., Int. Ed.*, 2007, **46**, 7778–7781.
- 12 H. Aono, E. Sugimoto, Y. Sadaoka, N. Imanaka and G.-y. Adachi, *Solid State Ionics*, 1990, **40**, 38–42.
- 13 N. Kamaya, K. Homma, Y. Yamakawa, M. Hirayama, R. Kanno, M. Yonemura, T. Kamiyama, Y. Kato, S. Hama and K. Kawamoto, *Nat. Mater.*, 2011, **10**, 682–686.
- 14 I.-H. Chu, H. Nguyen, S. Hy, Y.-C. Lin, Z. Wang, Z. Xu, Z. Deng, Y. S. Meng and S. P. Ong, *ACS Appl. Mater. Interfaces*, 2016, **8**, 7843–7853.
- 15 M. V. Reddy, C. M. Julien, A. Mauger and K. Zaghib, *Nanomaterials*, 2020, **10**, 1606.
- 16 A. Sakuda, A. Hayashi and M. Tatsumisago, *Sci. Rep.*, 2013, **3**, 1–5.
- 17 K. J. Kim, M. Balaish, M. Wadaguchi, L. Kong and J. L. Rupp, *Adv. Energy Mater.*, 2021, **11**, 2002689.
- 18 X. Li, J. Liang, X. Yang, K. R. Adair, C. Wang, F. Zhao and X. Sun, *Energy Environ. Sci.*, 2020, **13**, 1429–1461.
- 19 T. Asano, A. Sakai, S. Ouchi, M. Sakaida, A. Miyazaki and S. Hasegawa, *Adv. Mater.*, 2018, **30**, 1803075.
- 20 X. Li, J. Liang, J. Luo, M. N. Banis, C. Wang, W. Li, S. Deng, C. Yu, F. Zhao and Y. Hu, *Energy Environ. Sci.*, 2019, **12**, 2665–2671.
- 21 R. Schlem, S. Muy, N. Prinz, A. Banik, Y. Shao-Horn, M. Zobel and W. G. Zeier, *Adv. Energy Mater.*, 2020, **10**, 1903719.
- 22 K.-H. Park, K. Kaup, A. Assoud, Q. Zhang, X. Wu and L. F. Nazar, *ACS Energy Lett.*, 2020, **5**, 533–539.
- 23 H. Kwak, D. Han, J. Lyoo, J. Park, S. H. Jung, Y. Han, G. Kwon, H. Kim, S. T. Hong and K. W. Nam, *Adv. Energy Mater.*, 2021, **11**, 2003190.
- 24 L. Zhou, C. Y. Kwok, A. Shyamsunder, Q. Zhang, X. Wu and L. F. Nazar, *Energy Environ. Sci.*, 2020, **13**, 2056–2063.
- 25 H. Chun, K. Nam, S. J. Hong, J. Kang and B. Han, *J. Mater. Chem. A*, 2021, **9**, 15605–15612.
- 26 J. Liang, X. Li, S. Wang, K. R. Adair, W. Li, Y. Zhao, C. Wang, Y. Hu, L. Zhang and S. Zhao, *J. Am. Chem. Soc.*, 2020, **142**, 7012–7022.
- 27 Y. Huang, Y. Yu, H. Xu, X. Zhang, Z. Wang and G. Shao, *J. Mater. Chem. A*, 2021, **9**, 14969–14976.
- 28 L. Zhou, T.-T. Zuo, C. Y. Kwok, S. Y. Kim, A. Assoud, Q. Zhang, J. Janek and L. F. Nazar, *Nat. Energy*, 2022, **7**, 83–93.
- 29 K. Kim, D. Park, H.-G. Jung, K. Y. Chung, J. H. Shim, B. C. Wood and S. Yu, *Chem. Mater.*, 2021, **33**, 3669–3677.
- 30 Y. Nikodimos, W.-N. Su, H. Bezabh, M.-C. Tsai, C.-C. Yang and B. Hwang, *Mater. Today Chem.*, 2022, **24**, 100837.
- 31 W. M. Haynes, D. R. Lide and T. J. Bruno, *CRC handbook of chemistry and physics*, CRC Press, 2016.
- 32 G. Kresse and J. Furthmüller, *Phys. Rev. B: Condens. Matter Mater. Phys.*, 1996, **54**, 11169.
- 33 G. Kresse and D. Joubert, *Phys. Rev. B: Condens. Matter Mater. Phys.*, 1999, **59**, 1758.
- 34 J. P. Perdew, K. Burke and M. Ernzerhof, *Phys. Rev. Lett.*, 1996, **77**, 3865.
- 35 H. Xu, D. Cheng, D. Cao and X. C. Zeng, *Nat. Catal.*, 2018, **1**, 339–348.
- 36 Z. Zhu, Z. Deng, I.-H. Chu, B. Radhakrishnan and S. Ping Ong, in *Computational Materials System Design*, Springer, 2018, pp. 147–168.
- 37 S. P. Ong, W. D. Richards, A. Jain, G. Hautier, M. Kocher, S. Cholia, D. Gunter, V. L. Chevrier, K. A. Persson and G. Ceder, *Comput. Mater. Sci.*, 2013, **68**, 314–319.
- 38 G. Henkelman and H. Jónsson, *J. Chem. Phys.*, 2000, **113**, 9978–9985.
- 39 Z. Zhang, Z. Zou, K. Kaup, R. Xiao, S. Shi, M. Avdeev, Y. S. Hu, D. Wang, B. He and H. Li, *Adv. Energy Mater.*, 2019, **9**, 1902373.
- 40 N. J. de Klerk, E. van der Maas and M. Wagemaker, *ACS Appl. Energy Mater.*, 2018, **1**, 3230–3242.
- 41 K. Jun, Y. Sun, Y. Xiao, Y. Zeng, R. Kim, H. Kim, L. J. Miara, D. Im, Y. Wang and G. Ceder, *Nat. Mater.*, 2022, 1–8.
- 42 L. Pauling, *J. Am. Chem. Soc.*, 1929, **51**, 1010–1026.
- 43 K. Okhotnikov, T. Charpentier and S. Cadars, *J. Cheminf.*, 2016, **8**, 1–15.
- 44 Y. Liu, S. Wang, A. M. Nolan, C. Ling and Y. Mo, *Adv. Energy Mater.*, 2020, **10**, 2002356.
- 45 P. Di Pietro and A. Kerridge, *Phys. Chem. Chem. Phys.*, 2016, **18**, 16830–16839.
- 46 W. Baur, *Acta Crystallogr., Sect. B: Struct. Crystallogr. Cryst. Chem.*, 1974, **30**, 1195–1215.